Ceramic micro-injection molded nozzles for serial femtosecond crystallography sample delivery

K. R. Beyerlein, L. Adriano, M. Heymann, R. Kirian, J. Knoška, F. Wilde, H. N. Chapman, and S. Bajt

---

Articles you may be interested in

Possibilities for serial femtosecond crystallography sample delivery at future light sourcesa)
Struct. Dyn. **2**, 041709 (2015); 10.1063/1.4921220

A split-beam probe-pump-probe scheme for femtosecond time resolved protein X-ray crystallography
Struct. Dyn. **2**, 014102 (2015); 10.1063/1.4906354

Design and Construction of a High-speed Network Connecting All the Protein Crystallography Beamlines at the Photon Factory
AIP Conf. Proc. **879**, 1936 (2007); 10.1063/1.2436452

High Throughput Protein Crystallography at RIKEN Structural Genomic Beamlines
AIP Conf. Proc. **705**, 1209 (2004); 10.1063/1.1758017

Automation of Protein Crystallography Facilities at the SRS
AIP Conf. Proc. **705**, 1205 (2004); 10.1063/1.1758016

Ceramic micro-injection molded nozzles for serial femtosecond crystallography sample delivery

K. R. Beyerlein,[1] L. Adriano,[2] M. Heymann,[1] R. Kirian,[1,a)] J. Knoška,[3] F. Wilde,[4] H. N. Chapman,[1,3,5] and S. Bajt[2,b)]

[1]*Center for Free-Electron Laser Science, Deutsches Elektronen-Synchrotron, Notkestraße 85, 22607 Hamburg, Germany*
[2]*Photon Science, Deutsches Elektronen-Synchrotron, Notkestraße 85, 22607 Hamburg, Germany*
[3]*Department of Physics, University of Hamburg, Luruper Chaussee 149, 22607 Hamburg, Germany*
[4]*Helmholtz-Zentrum Geesthacht, Max-Planck-Straße 1, 21502 Geesthacht, Germany*
[5]*Centre for Ultrafast Imaging, Notkestraße 85, 22607 Hamburg, Germany*

Serial femtosecond crystallography (SFX) using X-ray Free-Electron Lasers (XFELs) allows for room temperature protein structure determination without evidence of conventional radiation damage. In this method, a liquid suspension of protein microcrystals can be delivered to the X-ray beam in vacuum as a micro-jet, which replenishes the crystals at a rate that exceeds the current XFEL pulse repetition rate. Gas dynamic virtual nozzles produce the required micrometer-sized streams by the focusing action of a coaxial sheath gas and have been shown to be effective for SFX experiments. Here, we describe the design and characterization of such nozzles assembled from ceramic micro-injection molded outer gas-focusing capillaries. Trends of the emitted jet diameter and jet length as a function of supplied liquid and gas flow rates are measured by a fast imaging system. The observed trends are explained by derived relationships considering choked gas flow and liquid flow conservation. Finally, the performance of these nozzles in a SFX experiment is presented, including an analysis of the observed background. © *2015 Author(s). All article content, except where otherwise noted, is licensed under a Creative Commons Attribution 3.0 Unported License.* [http://dx.doi.org/10.1063/1.4936843]

I. INTRODUCTION

Serial femtosecond crystallography (SFX)[1] uses femtosecond X-ray pulses produced by an X-ray Free-Electron Laser (XFEL) to collect diffraction patterns from crystals to study their internal molecular structure. The X-ray pulses are intense enough to ionize a large proportion of the atoms in the sample multiple times. The rapid ionization leads to the formation of a plasma and the explosion of the sample.[2] However, with a sufficiently short X-ray pulse, diffraction patterns can be collected before the onset of significant atomic motion. Depending on the intensity, pulses longer than about 30 fs cause structural disorder that is largely filtered out of the data by the fact that only Bragg peaks are measured.[3,4] This method is opening new doors in structural biology, yielding atomic resolution structures from micrometer-sized crystals and smaller, radiation sensitive protein crystals,[5–10] as well as, enabling experiments to study fast structural protein dynamics.[11–15] Considering the destructive nature of the pulses, data collection is optimized by a serial approach, where a new crystal is placed in the beam for each X-ray pulse. The Linac Coherent Light Source (LCLS) FEL has the fastest repetition rate of all currently operational hard X-ray FELs at 120 Hz, but a much faster 4.5 MHz bunch mode will be implemented at

the European XFEL, which is currently under construction in Hamburg, Germany. Furthermore, as protein crystal samples are precious, sensitive to solvation conditions and difficult to produce, they should be delivered in their native growth medium in such a way as to minimize their consumption.

Since the conception of the SFX technique, micro-jets have been used for sample delivery, as the crystals can be delivered in a fast, micrometer-sized stream of the crystallization buffer that is positioned to intersect the X-ray focus in a vacuum environment. Early on, Rayleigh jets were found to be ineffective, as they require high flow rates, form ice when run in vacuum, and are prone to clogging with a suspension of protein crystals.[16] This led to the development of flow-focusing nozzles, which rely on a coaxial focusing gas to produce the micrometer-diameter liquid jet.[17,18]

Early experimental and theoretical investigations of flow-focusing were carried out by the group of Gañán-Calvo.[19–23] In many of their studies, flow-focusing was achieved by drawing air through a small orifice in a flat metal plate (flat-plate apparatus), and forming a jet from a capillary precisely positioned above the orifice.[24] The original apparatus was later miniaturized, replacing the plate with a surrounding outer borosilicate capillary that was flame polished at one end to produce a smooth convergent aperture.[17,18,21] This miniaturized design has been referred to as a gas dynamic virtual nozzle (GDVN), and a general schematic of one is shown in Figure 1. However, flame polished glass capillaries are fragile and prone to considerable variability in their manufactured geometry, including different diameters and straightness along

---

a)Current address: Department of Physics, Arizona State University, P.O. Box 871504, Tempe, Arizona 85287, USA.
b)Author to whom correspondence should be addressed. Electronic mail: sasa.bajt@desy.de.
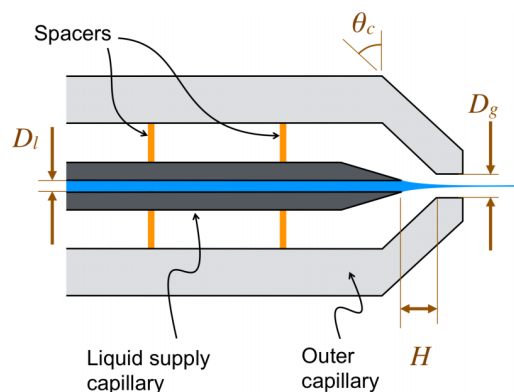
FIG. 1. Schematic of a gas dynamic virtual nozzle tip, identifying its various parts and geometric parameters and showing how they are arranged in a nozzle. The gas supply capillary is not shown in the drawing as it is normally positioned far away from the tip. The drawing is not to scale, see the text for details concerning nozzle dimensions. The gas aperture diameter is D_g, the inner diameter of the liquid supply capillary is D_l, the tip to aperture distance is H, and the capillary tapering angle is θ_c. The liquid is shown in blue, flowing from left to right. In a SFX experiment, the X-ray beam impinges the jet approximately at a right angle.

the convergent aperture, often resulting in a cross section that does not have ideal axial symmetry.[21] This can result in non-optimal gas flow streams, causing decentering of the liquid supply capillary relative to the gas aperture, and a different optimum distance of the capillary orifice to the nozzle exit—all of which have been shown to be important in the performance of flow-focusing nozzles.[20,21,23]

To improve nozzle reproducibility while reducing fabrication complexity, we investigated ceramic micro-injection molding to mass-produce high precision outer capillaries for GDVNs. Micro-injection molding can fabricate items of varying length scales, including features with dimensions of a few micrometers on parts which are centimeters in length. The small micrometer-sized jets, which are desirable for the SFX application, require the use of apertures in the range of 10-100 μm in diameter. During operation, stresses as high as 10 MPa can be applied to this aperture by the focusing gas. Because of their high compression strength (50-500 MPa) and elastic modulus (1-10 GPa), ceramics are suitable materials for such applications. In addition to an increased mechanical stability, ceramic micro-injection molded nozzles offer more chemical stability than those produced from polydimethyl-siloxane (PDMS) using soft-lithography[25]—enabling their use with a wider range of solvents.

The present manuscript details the design, assembly, and testing of our ceramic micro-injection molded nozzles and is organized as follows. A brief review of the theory concerning the relationship between the nozzle geometry and expected performance is given as a motivation for our design. This is followed by a detailed description of the nozzle design and assembly. The jet characteristics resulting from this design and their dependencies on the supplied liquid and gas flow rates in a laboratory setup are demonstrated and discussed. Furthermore, experimental data obtained at an X-ray FEL using our ceramic micro-injected nozzles are presented, focusing on a discussion of the background levels from the nozzle. The manuscript concludes with a summary of the results and ideas for future utilization of ceramic nozzles.

II. NOZZLE GEOMETRY INFLUENCE ON JET CHARACTERISTICS

The internal geometry of a GDVN determines the gas and liquid flow regimes of a stable jet. When using GDVNs to deliver precious protein samples in SFX experiments, one of the most important parameters is the minimum liquid flow rate, Q_{min}, as it determines the rate of sample consumption and the smallest achievable jet diameter (further discussed in the next paragraph). The study of Vega *et al.*[23] found empirically that the optimum minimum flow rate to produce a jet for low viscosity fluids is given by the relationship

$$\frac{Q_{min}}{D_g} = 2.5 \left(\frac{D_l}{D_g} \right)^{1/3} \mu/\rho, \tag{1}$$

where D_g and D_l are the gas aperture and liquid capillary inner diameters, respectively, μ is the liquid viscosity, and ρ is the liquid density. This minimum flow was obtained when the liquid supply capillary was positioned a distance, H, away from the gas aperture given by

$$\frac{H}{D_g} = 0.6 \left(\frac{D_l}{D_g} \right)^{1/4}. \tag{2}$$

When the capillary was positioned closer, the nozzle tended to atomize the stream through a process called flow blurring. At further distances, a higher liquid flow rate was necessary to produce a stable jet. From Equations (1) and (2), it is also evident that the geometric parameter that has the greatest effect on the flow properties is the diameter of the gas aperture, D_g. Later studies demonstrated that these relationships also hold for convergent gas aperture nozzles[19] and investigated scaling relationships for high viscosity fluids.[22] Although these empirical relationships were obtained for jets formed in air, they form a basis for characterizing jets in vacuum as described in Sec. IV.

Another important jet parameter to consider when designing nozzles for SFX experiments is the jet diameter. This is linked to critical experimental quantities such as the sample hit rate (fraction of X-ray pulses that hit a crystal), sample consumption efficiency (fraction of crystals hit by an X-ray pulse), and intensity of background signal from the protein crystal solvent. The functional dependence of the jet diameter on these quantities is found considering two cases: when the jet diameter, D_j, is either (1) larger or (2) smaller than the X-ray beam diameter, D_b. Considering a homogeneously dispersed crystal solution, continuously flowing from a nozzle, the crystal hit rate, f_h, is given by the product of the crystal concentration, ρ_c and irradiated volume, resulting in the respective expressions for cases 1 and 2,

$$f_h = \frac{\pi}{4} \rho_c D_b^2 D_j, \quad f_h = \frac{\pi}{4} \rho_c D_b D_j^2. \tag{3}$$

The sample consumption efficiency, f_s, comes from the ratio of the hit rate and the crystal flow rate, the latter given as the product of the crystal concentration and liquid flow rate, Q_l. The liquid flow rate is related to the jet diameter and velocity, v_j, by

$$Q_l = \frac{\pi}{4} D_j^2 v_j. \tag{4}$$

Using this expression, the sample efficiency is found to be independent of crystal concentration, and given for the two cases as

$$f_s = \frac{D_b^2 \nu_{Xray}}{D_j v_j}, \quad f_s = \frac{D_b \nu_{Xray}}{v_j}, \tag{5}$$

where ν_{Xray} denotes the X-ray pulse repetition rate. Finally, the measured background from solvent scattering is proportional to the irradiated volume. This quantity is expressed in Equation (3); therefore, the background increases linearly with jet diameter for case 1, and quadratically for case 2.

Comparing these relations, it is clear that a smaller jet can improve sample consumption efficiency and decrease background, with the tradeoff of reducing the hit rate for a constant sample concentration. In some cases, the sample concentration can be increased to make up for the loss in hit rate. However, this strategy also has limits, as sample concentrations above 10^{10} crystals/ml that are often necessary for experiments have been observed to cause jet instability. Nonetheless, the amount of protein crystals that can be produced is often the limiting factor in serial protein crystallography experiments. Therefore, a small jet is often desirable as it maximizes the number of diffraction patterns collected from a given volume of sample and improves the signal to noise by decreasing the background in the patterns.

Designing a nozzle that produces small jets requires understanding the fluid mechanics governing the jet formation process. Gañán-Calvo[24] has shown that the kinetic energy per unit volume in a jet is equal to the pressure difference across the nozzle aperture, ΔP_g, resulting in the relationship

$$\Delta P_g = \frac{8\rho_l Q_l^2}{\pi^2 D_j^4} = \frac{\rho_l v_j^2}{2}. \tag{6}$$

Use of this relationship requires knowledge of the pressure of the focusing gas inside the nozzle, which is dramatically different than the pressure applied to the gas supply capillary, due to the compressibility of gas. A more general relationship in terms of the gas mass flow can be found by combining Equation (6) with known relationships governing the flow of compressible gasses through an aperture. For a given pressure inside the nozzle, P_i, the mass flow rate of the gas is given by

$$Q_g = P_i A \sqrt{\frac{km_g}{RT}} \frac{M}{\left(1 + \frac{k-1}{2}M^2\right)^{\frac{k+1}{2(k-1)}}}, \tag{7}$$

where A is the cross-sectional area of the gas aperture, R denotes the ideal gas constant, T, the temperature, $k = C_p/C_v$, the ratio of specific heats of the gas, and m_g, the molar mass of the gas.[26] The variable M denotes the Mach number of the gas flow through the aperture and is defined as the gas velocity divided by its speed of sound. The speed of sound is the upper limit at which gas can pass through an aperture. At this speed, the flow is said to be choked or critical. For most gases, including helium, the flow of the gas through a nozzle becomes choked when $P_i/P_o \gtrsim 2$, where again P_i is the pressure inside the nozzle, and P_o is the pressure outside the nozzle. When this ratio is less than two, the Mach number

is given by the relationship[26]

$$M = \left\{\left[\left(\frac{P_i}{P_o}\right)^{\frac{k-1}{k}} - 1\right] \frac{2}{k-1}\right\}^{1/2}, \tag{8}$$

otherwise, for choked flow, $M = 1$. Then, from Equation (7), we define the velocity

$$\alpha = \sqrt{\frac{RT}{km_g}} \frac{\left(1 + \frac{k-1}{2}M^2\right)^{\frac{k+1}{2(k-1)}}}{M}, \tag{9}$$

and solving for the internal nozzle pressure, we obtain

$$P_i = \alpha p_g, \tag{10}$$

where $p_g = Q_g/A$ is the momentum of the gas flow through the aperture per unit volume. For choked flow, Equation (9) predicts a velocity of 1088 m/s for helium at STP, which is approximately its speed of sound. Equation (10) can then be used in Equation (6) in place of the internal nozzle pressure. Solving for the velocity of the jet results in the relationship

$$v_j = \sqrt{\frac{2(\alpha p_g - P_o)}{\rho_l}}. \tag{11}$$

When the pressure outside the nozzle is small with respect to the pressure inside, the factor P_o in this expression can be disregarded. In this case, it becomes evident that the velocity of the jet is proportional to the square root of the gas momentum through the aperture and the gas mass flow rate. One can also substitute Equation (10) into Equation (6) and solve for the jet diameter, finding

$$D_j = \left[\frac{8\rho_l}{\pi^2 (\alpha p_g - P_o)}\right]^{\frac{1}{4}} Q_l^{\frac{1}{2}}. \tag{12}$$

This expression suggests that the diameter of the jet will get smaller with increasing gas flow, but is more strongly dependent on the liquid flow.

In Section IV, measurements will be described to test the trends in jet diameter and velocity predicted by Equations (11) and (12). These tests are done in a vacuum of 10 Pa; therefore, choked flow can be expected if the pressure inside the nozzle exceeds 20 Pa. We are confident that it is actually above 100 kPa for all presented operating conditions because we have observed gas flowing out of the nozzle when it is taken out of vacuum and held at STP conditions: 300 K and 100 kPa. The preceding equations can be utilized assuming a choked gas flow, or $M = 1$. Furthermore, in the case of choked flow, lowering the pressure outside of the nozzle beyond the critical pressure will not change the flow inside the nozzle, only changing internal pressure can have an effect.[26] Therefore, the reported performance of the nozzle is expected to be the same at lower chamber pressures, such as the conditions of the measurements taken at LCLS presented in Section V.

III. NOZZLE DESIGN AND ASSEMBLY

The general scaling dependencies of Equations (1) and (2) are helpful when designing a GDVN. From this
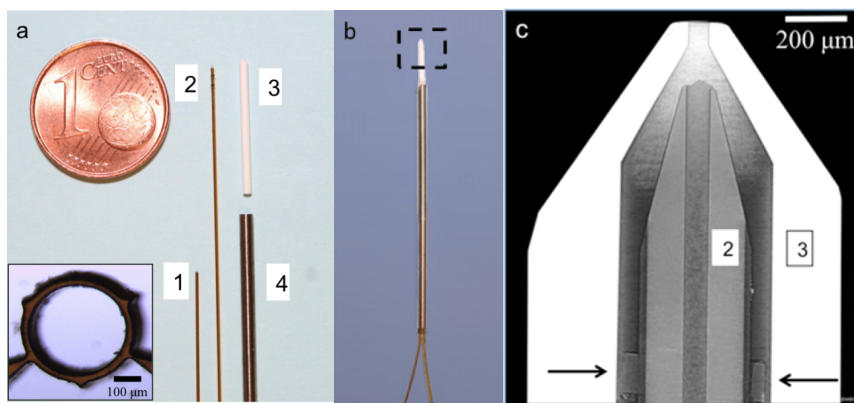
FIG. 2. The parts used to assemble the nozzle are depicted (a): (1) gas supply capillary, (2) liquid supply capillary, (3) ceramic injection molded outer capillary, and (4) stainless-steel assembly tube. The inset of (a) shows a microscopic image of a laser-cut Kapton spacer before placement on a liquid capillary. Also shown is an image of an assembled nozzle (b) with the tip indicated by a dashed box. A rendering of an x-ray tomogram of this tip shows details of the internal geometry of a nozzle where the jet is formed (c). The nozzle components in this image are labeled in the same scheme as described for (a). Arrows indicate a Kapton spacer visible in this image. The gas supply capillary is outside the view as it is typically positioned centimeters away from the gas aperture.

aforementioned theory and our experience in making nozzles by the flame-polishing technique, an outer capillary suitable for ceramic micro-injection molding was designed. The general shape of the designed outer capillary follows that depicted in Figure 1, and images of an example outer capillary are shown in Figure 2. A gas aperture diameter of $D_g = 70$ μm was chosen to allow for the use of liquid supply capillaries with inner diameters, D_l, from 10 to 75 μm. Using Equation (2), our design was optimized for a tip-to-aperture distance of $H \approx 50$ μm, which Equation (1) predicts will result in a minimum flow rate around 10 μl/min. While this setup optimizes the performance in terms of flow rate, as will be discussed later, we have ultimately found out that a slightly larger distance is more suitable for SFX experiments as it improves the jet stability and straightness without dramatically changing the flow rate for a jet. The tapering angle θ_c of the capillary was chosen to be 60° that is beyond the current maximum collection angle of 45°. The 500 μm inner diameter of the ceramic outer capillary limited its maximum length to 16 mm due to limitations of the molding process. A longer length is desirable as it allows for easier interfacing and assembly of the nozzle. An outer diameter of 1 mm was chosen to match preexisting nozzle assembly tubes. The ceramic outer capillaries were manufactured by Small Precision Tools (SPT, Switzerland), using a mixture of corundum (Al_2O_3) and zirconia (ZnO_2). The gas aperture of each ceramic capillary was inspected with an optical microscope prior to its use as a nozzle, and a mean gas aperture of 71.5 μm with a standard deviation of 2.5 μm was measured from 20 delivered pieces.

Our ceramic outer capillaries replaced the flame polished glass capillaries when assembling GDVNs according to the procedure described by DePonte *et al.*[17] The parts of a nozzle discussed in this paragraph are shown in Figure 2(a). For the liquid supply, polymicro-fused silica capillaries with an outer diameter of 352 ± 2 μm, measured by a scanning laser micrometer (LaserLinc, Inc.), and inner diameters D_l of either 20, 30, 50, or 75 μm were used. Before assembly, the liquid capillaries were sharpened to a point by wet mechanical polishing with a half angle of 18°. In some cases, the sharpened

tips were dipped into pure hydrofluoric acid (40%), for 15 s to slightly etch the exposed glass and smooth the ground surface. Then, two Kapton rings with an inner diameter of 350 μm and an outer diameter of 500 μm (hereafter referred to as spacers) were placed on the liquid supply capillary to coaxially align it with the outer capillary, as illustrated in Figure 1. These rings were precision laser cut (LLT Applikation GmbH, Ilmenau, Germany) from a 100 μm thick Kapton film (DuPont). Three legs were carved out of the outer edge of the rings to allow gas to flow around them.[27] A micrograph of a spacer mounted in the Kapton film is shown in the inset of Figure 2(a). Focusing gas was supplied to the GDVN by a second polymicro-fused silica glass capillary of 100 μm inner diameter inserted into the outer capillary through the back of the assembly. The inner and outer capillaries could be assembled and sealed together using either a screwed-together nozzle holder[16] or a stainless-steel metal tube of 1 mm inner and 1.58 mm outer diameter. Typically, liquid and gas capillaries were around 2 m long. This length is needed to connect our nozzles located inside the experiment chamber to external sample reservoirs and injection system using equipment like that at the Coherent X-ray Imaging (CXI) instrument of the LCLS.[18]

After rough assembly, nozzle parts were carefully aligned with a dedicated micrometer fiber alignment stage (Thorlabs, Part No. MBT610D) before they were fixed in place. The stage enabled precise positioning of the liquid capillary tip to the gas aperture distance, H. Once the desired distance was achieved, the gas and liquid capillaries were secured in place by gluing them in the metal tube with two-component epoxy. A fully assembled nozzle is shown in Figure 2(b). Assembled nozzles were then tested for their performance as detailed in Sec. IV. Poorly performing nozzles were easily recycled by burning the epoxy away using a flame. Due to their high thermal stability, the ceramic outer capillaries remained undamaged and could be assembled into a new nozzle.

As our zirconia and alumina ceramic outer capillary is not transparent and hence not compatible with optical microscopy, we used X-ray tomography to visualize the final internal geometry of assembled nozzles. When seeing inside the nozzle

with visible light is critical, the piece can also be made with translucent alumina. Figure 2(c) shows a rendering of an X-ray tomogram of the tip of an assembled nozzle having a liquid capillary inner diameter of 75 μm. A full tomogram of the tip was recorded, which shows the full internal geometry of the nozzle tip in three-dimensions. The tomogram was taken using a Phoenix Nanotom S instrument (General Electric Company) with an X-ray tube operating at 45 kV on a Mo target. The tomogram was reconstructed from 2400 projections in a 360° rotation scan about the cylindrical axis of the nozzle. The distance H for this nozzle was measured from the tomogram to be 110 μm. The contrast in Figure 2(c) is good enough to show small details such as the laser-cut Kapton spacer that is visible at the bottom of the image. The rendering also clearly shows that the tip of the liquid capillary has an uneven rim. This feature was not intentional, but can happen during the nozzle assembly process due to the fragility of the thin glass walls that are formed. In Sec. IV, we will present the performance of this nozzle, showing that it generally agrees with the derived models for jet size and velocity. Therefore, it is believed that this amount of rim unevenness results in a nozzle performance that is still suitable for our experiments.

IV. CHARACTERIZATION OF NOZZLE PERFORMANCE

The performance of GDVNs made with our ceramic outer capillaries was assessed using the optical microscopy setup depicted in Figure 3. hThe nozzles were tested in a chamber with rough vacuum conditions to simulate a SFX experiment. The chamber is made of a KF-40 aluminum nipple with two side windows cut out and glass microscope slides glued over the gaps. These windows enabled illumination and imaging of the nozzle during the operation in the chamber. The chamber was attached to an Edmunds XDS35 scroll pump, and an O-ring seated on the back of the nozzle provided a sufficient seal for the vacuum and was firm enough to hold the nozzle in place. During the operation of a nozzle, typical chamber pressures were in the range of 10 Pa, while the base pressure of the pump was around 0.1 Pa.

Jet stability and breakup were imaged using a Photron FASTCAM SA4 camera, which can take up to 500 000 frames per second with a shutter speed of 1 microsecond. For 10 μm droplets, this shutter speed allows for clear snapshot images of the jet and droplets traveling at a speed of 10 m/s. The optics consisted of a Navitar 12× Ultra-Zoom motorized lens and a 10× Mitutoyo objective lens, which allowed for a resolution from 0.3 to 3 μm/pixel. Illumination was produced by a Karl Storz xenon lamp coupled to a liquid light guide or a LDX Optronics 250 mW multi-mode fiber coupled 635 nm laser diode powered by a Newport LDP-3830 supply. The xenon lamp provides a more uniform background, while the pulsed laser source provides a faster time resolution. To image smaller and faster droplets, we used the pulsed laser diode with a 500 ns pulse duration (flat-top pulses), which allows clear imaging of droplets at speeds up to 20 m/s. The image brightness was the major factor limiting the pulse duration, and shorter pulses can be used with a lower magnification to observe the stability of a faster jet. A ground glass diffuser was placed between the laser
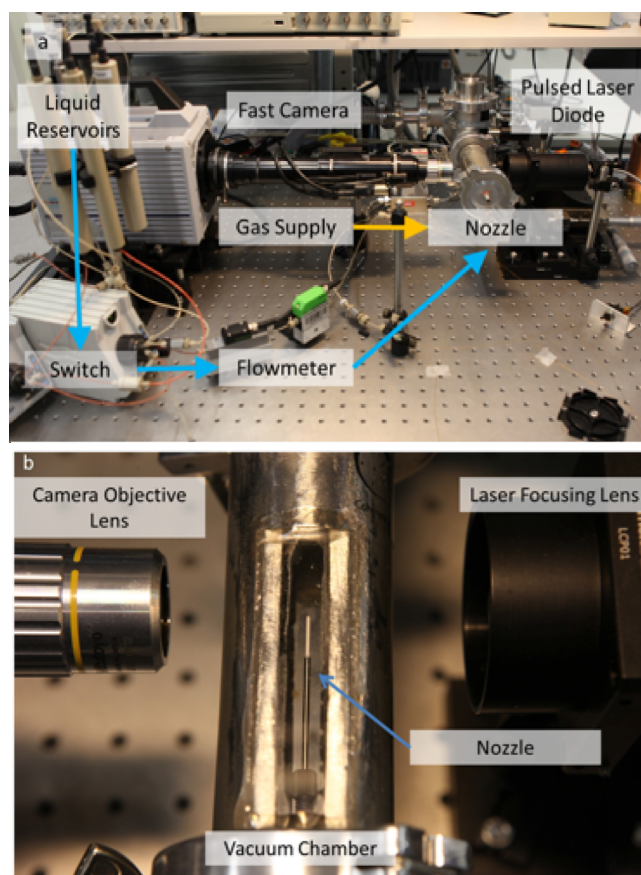

FIG. 3. The layout of the testing station used to characterize nozzles under vacuum is shown in (a). Also depicted are a nozzle inserted into the vacuum chamber and a close up of the objective lens and illumination optics (b). In this image, the testing chamber is rotated 90° from its normal operating orientation to show the windows and view through the chamber.

and the test chamber as needed to reduce the speckle from the laser diode observed in the images.

Liquid was supplied to the nozzle by pressurizing a polyether ether ketone (PEEK) cylinder filled with the liquid sample. The pressurizing gas was controlled by a Parker high-pressure self-relieving regulator installed upstream of the reservoir. In the following tests, helium was used, but the choice of gas used to pressurize the liquid reservoir is not critical as nitrogen is also often used without an observed change in the nozzle performance. Alternatively, we also used a high-pressure liquid chromatography pump or a high-pressure syringe pump to supply liquid to the nozzle resulting in comparable nozzle performance. However, we have found that the pressurized reservoir system offered the best flow stability and sensitivity over a large range of flow rates. It can be difficult to load fluids into syringe pumps without gas bubbles. When this happens, it causes a slow response time when changing the flow rate. The volumetric flow of the liquid into the nozzle was measured with one of two flow meters installed in series along the liquid line—the Sensirion SLG64-0075 for 2-20 μl/min flow rates or the Sensirion SLI-0430 for 5-80 μl/min flow rates. The precisions of these flow meters were, respectively, measured to be 3% and 10% of the measured flow rate, calibrated by weighing water collected over a period of 30 min at different flow rates. During testing,

a liquid pressure up to 10 MPa was typically applied to the reservoir. The corresponding flow, Q_l, through the nozzle then depended on the inner diameter of the liquid capillary. While both pressure and liquid flow were recorded, only flow through the nozzle will be presented here as this is the conserved quantity for an incompressible system, independent of the tubing used upstream of the nozzle.

Helium gas was supplied to the nozzle in a similar way, using a second Parker self-relieving pressure regulator connected to a Bronkhorst EL-Flow gas mass flow meter. Helium was chosen as the focusing gas because it helps to minimize X-ray background in two ways. First, background scattering from the focusing gas is low, as helium does not scatter X-rays strongly. Second, its high speed of sound maximizes jet speed, resulting in a thinner jet, and correspondingly reduced background due to X-ray scatter from the water column. In previous flow-focusing studies, the energy supplied by the gas flow to the system was described in terms of the gas pressure.[19,23,28] However, we will base our analysis on mass flow because this quantity is conserved throughout the nozzle, regardless if the flow is choked at the exit gas aperture.

In the present study, a stability test consisted of inserting a nozzle into the test chamber and observing the stability of the jet for different liquid and gas flow rates. Nozzles were first tested with water since it is the main solvent for most protein crystal solutions. The stability test began by flowing helium at a constant rate and then slowly increasing the liquid flow starting from zero. After allowing a few seconds for stabilization, the state of the jet was recorded. However, when the gas pressure was changed, the liquid flow would be first decreased to zero and then increased again in slow increments. By always starting the liquid flow from zero, the possibility of reporting erroneous jet stability due to well-known hysteresis in the dripping to jetting transition in flow-focusing nozzles[23] was reduced. The reported flow rates for the transitions are then upper limits, as transition flow rates that are in some cases as much as 5 μl/min lower can be obtained by starting from a higher flow rate and slowly lowering the liquid flow rate. However, in our experience, these states are only stable for a few minutes and not always reproducible, so reporting the upper limits of the transitions is more representative of the long-term stability of the jet. While the specific behavior of

the jet can be more complex, the state of the jet was classified into three general categories as follows:

- Dripping: the meniscus is not stable, and drops are quasi-periodically ejected from the nozzle.
- Jetting: a stable meniscus is present which is drawn into a slender jet.
- Whipping: the jet stream is spatially unstable, and "whips" around with an amplitude larger than its diameter.

An example of a water jet stability phase diagram obtained from the nozzle in Figure 2(c) is depicted in Figure 4(a). Figure 4(b) shows example images of the nozzle and jet in the various stability regimes taken with the pulsed laser illumination system. The stability behavior of the assembled nozzle qualitatively agrees with other such diagrams presented elsewhere.[19,29] However, a careful distinction must be made when comparing our stability phase diagram to these results. In some cases, the authors were primarily concerned with the stability of the liquid meniscus, called local stability. Our study is focused on the stability of an ejected liquid jet, often referred to as global stability, as this characteristic is more important for the application to SFX.

The phase diagram in Figure 4 shows that a jet is only stable above a minimum liquid flow rate and up to a certain maximum gas flow rate. For this particular nozzle, we determined that the jet was stable above a liquid flow rate of 12 μl/min and for a gas mass flow rate between 10 and 60 mg/min. At a gas flow rate above 60 mg/min, the jet became spatially unstable (whipping). The growth of these whipping oscillations along the length of the jet increased gradually with increased gas flow. The transition to the whipping state shown in Figure 4 was determined as the point where these oscillations became comparable to the diameter of the jet. Whipping has been postulated to be more prevalent in jets produced by nozzles constructed using tapered outer capillaries than for flat-plate apparatuses.[19] Nozzles for SFX applications have a converging conical outer wall to minimize shadowing of the measured diffraction pattern by clipping the diverging scattered X-rays with the nozzle, which means a convergent gas aperture is unavoidable even though it may be prone to whipping. This whipping instability defines the upper limit of
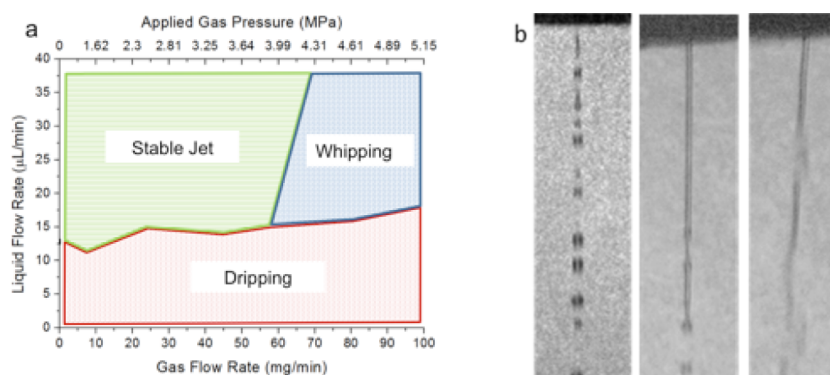

FIG. 4. The experimentally obtained jet stability phase diagram (a) shows three distinct regimes for a nozzle flowing water with a liquid capillary inner diameter of 75 μm. The gas mass flow rate and the pressure applied to the gas supply capillary are depicted. Also shown are example images of the jet (b) depicting a dripping jet (left), a stable jet (center), and a whipping jet (right). The jet in these images is flowing from top to bottom.
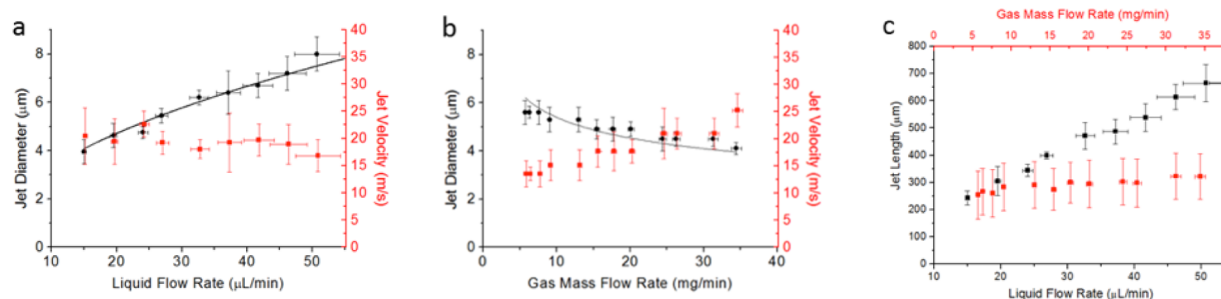
FIG. 5. The measured jet diameter (black circles) and corresponding jet velocity (red squares) as a function of liquid flow rate (a) and gas mass flow rate (b) are shown. The lines in these figures represent fits of the jet diameter assuming the dependence predicted by Equation (12). Also, the average measured jet length as a function of liquid flow rate (black squares) and gas mass flow rate (red circles) is shown in (c). The error bars on gas and liquid flow rates show the precision of the respective flow meters. The average value was obtained by averaging ten data points, so the standard errors of the measured flow rates are about three times smaller than the error bars. Please refer to the text for a description of how jet diameter and jet length error bars are calculated. The nozzle used in these experiments is the same as that depicted in Figure 2(c). All tests were performed with water. The measurements at different liquid flow rates were made with a constant gas mass flow rate of 20 mg/min, while those for different gas flows were made with a constant liquid flow rate of 20 μl/min.

the gas flow that can be used with this type of nozzle in a SFX experiment.

In the stable jetting regime, changing the liquid and gas flow rates influences the jet diameter and length. The effects of the liquid and gas flow on these parameters are depicted in Figure 5. The same nozzle as that previously studied was used for this test, and the reported diameters were measured at a point on the jet 15 μm from the orifice. The zoom lens position was set to achieve a pixel resolution of 0.3 μm/pixel for images of smaller jets and 0.5 μm/pixel for those of larger jets. As this resolution is close to the wavelength of light, the jet appeared as two parallel black lines with grey borders. The diameter was taken to be the average of the distance between the black lines and the distance between the grey borders, and the uncertainty was taken to be half the difference of these values—roughly two pixels wide. The jet velocity was also calculated from the measured jet diameters and liquid flow rates using a reformulation of Equation (4),

$$v_j = 4Q_l/\pi D_j^2. \tag{13}$$

These data are also plotted in Figures 5(a) and 5(b) as a function of the liquid and gas flow rates, respectively. The error bars of the jet velocity are the uncertainties propagated from the measured uncertainties of the jet diameter, which is the dominant error.

Figure 5(a) shows that as the liquid flow rate was increased between 10 and 60 μl/min with a constant gas flow rate, the jet diameter was found to increase from 4 to 8 μm, and the calculated jet velocity slightly decreased from 20 to 15 m/s. A fit of the jet diameter, assuming a $Q_l^{1/2}$ dependence following the prediction of Equation (12), is also shown in Figure 5(a) and is found to agree within the uncertainty of the measurement. Figure 5(b) shows that the jet diameter was also slightly sensitive to the gas mass flow rate, as the diameter decreased from 6 to 4 μm as the gas flow rate was increased between 5 and 35 mg/min, reflecting an increase in the average jet velocity from 12 to 25 m/s. These observed velocities are in fair agreement with those predicted by Equation (11) assuming choked flow, as a helium gas flow rate of 20 mg/min through a 70 μm aperture is predicted to result in a 14 m/s jet, while 17 ± 2 m/s was measured. A fit of the jet diameter trend assuming

the $Q_g^{-1/4}$ dependence predicted by Equation (12) is also shown in Figure 5(b) and seems to agree with the measured data.

Once the jet is formed, the jet length is governed by a breakup process similar to the Plateau-Rayleigh instability. The difference being that in the GDVN case, the focusing gas changes the axial velocity gradient of the liquid in the jet.[29] For experiments performed with X-ray beams, the jet length is of importance as it determines the maximum distance of the nozzle from the X-ray interaction region to intercept a contiguous jet. Intercepting the jet before it breaks up into droplets generally optimizes data collection efficiency, as will be discussed later. The measured jet length for different liquid and gas flows is shown in Figure 5(c). It was found that the jet length fluctuated significantly for sequential frames in a movie recorded at 30 000 frames per second. The values in Figure 5(c) are then the average jet lengths found with the error bars depicting the observed variation over a set of 100 sequential frames analyzed for each measurement condition. Given a constant gas flow, it was found that, along with the increase in jet diameter (Fig. 5(a)), an increase in the liquid flow rate results in a longer jet. In this case, a longer jet is explained by the longer time necessary for surface waves to grow large enough to pinch off the stream into droplets due to the increased jet diameter. Figure 5(c) also shows that the jet length is largely unaffected by the gas flow rate. The same behavior has also been observed for other nozzles tested with the fast imaging system. As shown in Figure 5(b), a higher gas flow results in a nearly two-fold increase in the jet speed and a less than 20% decrease of its diameter. One would then expect that such a jet would be about 50% longer, assuming a constant surface wave growth rate. However, the observation that the jet length is independent of the gas flow rate could be explained by a surface wave growth rate that increases with the gas mass flow rate, thus negating the effects of a faster jet.

The ceramic nozzle presented here shows typical behavior and stability ranges that meet the requirements of most SFX applications. We have assembled 180 nozzles with either a 50 μm or 75 μm inner diameter liquid capillary, of those 67% (122 nozzles) made a suitable jet. Limiting to the case of nozzles with 75 μm liquid capillaries that were ground with an 18° angle, 73% (68 of 93) formed a jet. Further considering those that were slightly etched with hydrofluoric acid, 13 out

of 14 nozzles formed a suitable jet—suggesting a possible route for further improvement of the nozzle stability. The main observed difference between assembled nozzles is that the produced jets are not perfectly coaxial with the nozzle, but have different degrees of angular deviation. Most likely this deviation indicates misalignment of the liquid capillary with respect to the gas aperture and is caused by an insufficient precision in the spacer dimensions and positioning. We found that the minimum liquid flow rate for a stable jet can be shifted towards lower values (~5 μl/min) by adjusting the distance of the liquid capillary to the gas aperture, H. This minimum flow rate is expected at the distance given by Equation (2).[23] However, we found that the stable jet regime becomes narrower with respect to the gas flow rate at this position compared with larger values of H. Also, when the liquid capillary is closer, the transition to whipping is more abrupt at a gas flow of around 30 mg/min. Finally, a smaller H also leads to a higher sensitivity of the jet to the capillary centering, resulting in an angular deviation of the jet as large as 30°. A plot of this angular deviation of the jet direction as a function of the observed minimum water flow rate for a set of different nozzles is shown in Figure 6. For our purposes, the optimum liquid capillary to gas aperture distance, H, for a SFX experiment is the smallest that leads to a straight and stable jet. For the ceramic capillary size and geometry we tested (shown in Figure 2), this distance is about twice the distance predicted by Equation (2) (~100 μm).

V. SAMPLE DELIVERY IN SFX EXPERIMENTS

In this section, we discuss the use of ceramic micro-injected nozzles during a SFX experiment. In such experiments, the sample is delivered to the focused X-ray beam by positioning the nozzle so that the liquid stream intersects the X-ray focus with the flow running perpendicular to the X-ray beam. The intersection is typically chosen in the continuous jet of a stable jet rather than the breakup region because the jet diameter is about half the average drop diameter—causing
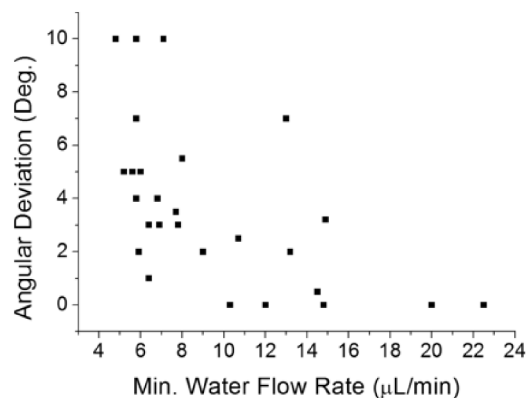

FIG. 6. The observed jet angular deviation from a perfect coaxial alignment is depicted for a set of assembled ceramic nozzles, which had different minimum water flow rates to produce a stable jet. Each point in the plot represents a different assembled nozzle from a set that was assembled with H ranging from 20 to 200 micrometers. The higher recorded flow rates correspond to nozzles assembled with a larger H, while those with lower flow rates were assembled with a smaller H.

half the background in the diffraction pattern due to X-ray scattering from the liquid. Furthermore, unless the droplet breakup is driven at a fixed frequency, the fraction of pulses that hit the sample is reduced in the droplet region. Since diffraction is recorded at high scattering angles, shadowing of the diffraction by the nozzle is a concern. The conical outer shape of the nozzle reduces the distance that the X-ray beam must be placed from the nozzle tip to avoid shadowing of the diffraction pattern. In our current design, the intersection point must be at least 65 μm from the tip to avoid shadowing at scattering angles below 30°. However, even for distances from the beam to the nozzle tip of 100 μm or more, high-angle X-ray scattering from the nozzle is often observed originating from a significant amount of X-ray intensity in the periphery of the X-ray focus profile. GDVNs with a glass outer capillary[16-18] add a diffuse background to X-ray diffraction patterns. In contrast, our ceramic nozzles consist of a mixture of crystalline ceramic phases and the background mainly consists of well-defined powder rings. Because ceramics strongly scatter high energy X-rays, we studied the background produced in an XFEL experiment to ensure that (i) the scattering will not cause damage to detectors and hence limit the X-ray flux used during the experiment and (ii) the collected data are not significantly influenced.

An experiment was conducted at the CXI instrument of LCLS using a focused 3 μm diameter X-ray beam at 6 keV.[30] The nozzle was placed in the shroud system installed at CXI which achieves a pressure of 0.01 Pa in the shroud and 10^{-5} Pa in the main chamber when a gas-focusing nozzle is in operation.[18] The nozzles used in the experiment performed the same in this chamber as they did in the rough vacuum testing system provided as part of the injector characterization lab (ICL) of LCLS. Different nozzles with either ceramic injection molded or glass flame-polished outer capillaries were used during the course of the experiment. The tip of the nozzle was positioned approximately 200 μm away from the X-ray focus, and flow rates in the range of 40 to 60 μl/min were necessary to form a long enough jet of the liquid suspension of protein microcrystals. The performance of the ceramic injection molded nozzles was comparable to the glass nozzles with regard to flow rates necessary for sample delivery. At one point during the experiment, a concentrated solution of lysozyme microcrystals[31] was flown in a ceramic nozzle producing a stable jet and yielding 13 000 diffraction patterns in just 13 min of data collection. A summation of these images after local background subtraction is shown in Figure 7(a). The signal from lysozyme is seen to extend to about 3 Å, and little evidence of shadowing or scattering from the ceramic nozzle is seen in the pattern.

During this experiment, it was observed that ice and other substances had poor adhesion to the surface of the ceramic nozzle. This allowed salt and protein debris that built up over time to be cleaned off the tip of the nozzle. When a significant amount of debris accumulated on the tip, we flushed the nozzle with water, then reduced the gas flow to zero. Since the nozzle was in vacuum, this caused ice formation at the tip, encapsulating the debris. Then by turning off the water and reinitiating the gas flow, the blob of ice and debris was quickly blown away, leaving a clean nozzle tip and a fully functional nozzle. If this procedure was found to be insufficient (as when the nozzle was
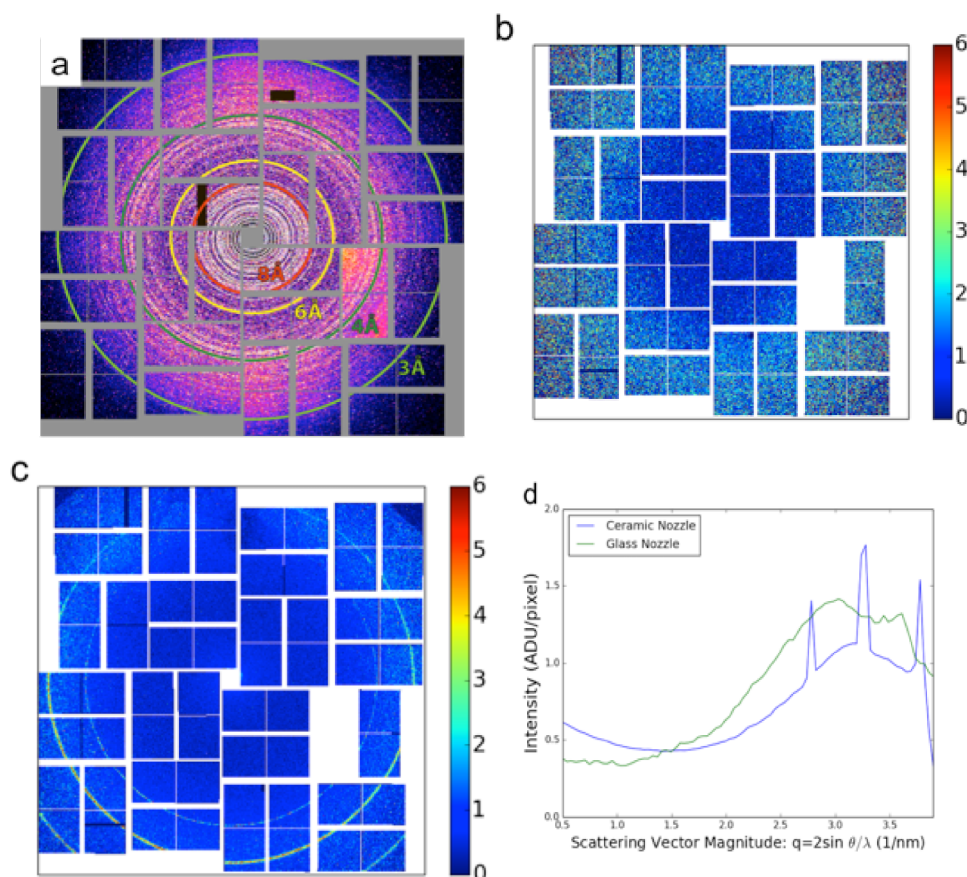
FIG. 7. The sum of more than 13 000 lysozyme diffraction patterns collected with a ceramic nozzle is shown in (a). Also, the average diffraction pattern backgrounds collected from glass (b) and ceramic (c) nozzles during an experiment at LCLS are compared. In each case, about 1000 patterns contributed to the average. The radial average of the bottom half of these background patterns (d) compares the scattering signal coming from these nozzles.

completely clogged with the sample, preventing its flushing with water), it was possible to clean the nozzle by removing it from the vacuum chamber and rinsing it with a few drops of water, or dipping the tip in an ultrasonic bath for a few seconds. Similar cleaning procedures can be used for GDVNs made with borosilicate glass outer capillaries, but the surface adhesion of ice and other substances in vacuum was found to be noticeably stronger.

Some of the experimental data were recorded when the nozzle was dripping. These data were then sorted into water *hits* and *misses* using the average intensity on a panel of the detector where the scattering signal from water is at its peak. *Hits* were the subset of collected diffraction patterns with a non-zero intensity in this panel caused by a water droplet intercepted by the X-ray beam, while *misses* were patterns formed by X-rays which pass through the interaction region without scattering from the sample stream. Figures 7(b) and 7(c) show averages of these *misses* taken from data collected using a glass nozzle and a ceramic nozzle, respectively. The observed signal in these patterns is attributed to the scattering of unfocused X-rays from the nozzle tip, and as such is a measure of the background signal coming from the nozzle. Figure 7 shows then the contrast between the diffuse signal from a nozzle with a glass outer capillary and the powder rings from a ceramic outer capillary nozzle, attributed to the corundum and zirconia phases. The powder rings from the ceramic nozzle slightly decrease in intensity toward the top

of the diffraction pattern due to shadowing, as the nozzle was placed into the interaction region from above.

The radial averages of the bottom half of the patterns in Figures 7(b) and 7(c) are shown in Figure 7(d), comparing the respective background level from each nozzle. The patterns have not been rescaled and reflect the average detected intensity per pixel as a function of the scattering vector. They show that the background from ceramic nozzles reaches a maximum background level at the Bragg condition similar to that of a glass nozzle. Therefore, data quality should not be affected by the use of a ceramic nozzle any more than that from a glass nozzle.

VI. SUMMARY AND DISCUSSION

We built and tested gas dynamic virtual nozzles made from ceramic micro-injection molded outer capillaries. These nozzles deliver predictable and stable jets reproducibly under operating conditions compatible with SFX experiments. Such a nozzle was assembled and characterized under various flow conditions. A stable jet of water was formed with a helium gas flow rate between 10 and 60 mg/min and a liquid flow rate starting at 12 μl/min. At higher gas flow rates, a whipping instability in the nozzle was observed, which is problematic for the application to SFX experiments. The jet length and diameter follow expected trends considering the geometrical and physical relationships that govern choked gas flow and

liquid flow conservation. No detrimental effects due to the ceramic nozzles have been observed in XFEL experiments to date.

In fact, the well-defined powder pattern from ceramic nozzles could in some cases even be a benefit as opposed to the higher diffuse background resulting from a glass nozzle. For instance, if the signal from the sample is diffuse, as in the case of solution scattering,[12] the sharp rings from the ceramic nozzle will produce a distinct background signal, which can be masked or subtracted on a per image basis. Removal of the diffuse ring background coming from a glass nozzle is more complicated as it affects more pixels and overlaps with the signal from the solution.

The feature resolution and reproducibility of micro-injection molding allow for easier and faster manufacture of nozzles producing micrometer-sized jets. Smaller, stable jets at lower flow rates are within reach by further reducing the gas aperture size and optimizing other nozzle design parameters. Finally, ceramic micro-injection molded pieces may also be of interest in other high-pressure sample delivery systems used in SFX experiments, such as an injector for protein crystals embedded in lipidic cubic phase.[32]

[1]H. N. Chapman, P. Fromme, A. Barty, T. A. White, R. A. Kirian, A. Aquila, M. S. Hunter, J. Schulz, D. P. Deponte, U. Weierstall, R. B. Doak, F. R. N. C. Maia, A. V. Martin, I. Schlichting, L. Lomb, N. Coppola, R. L. Shoeman, S. W. Epp, R. Hartmann, D. Rolles, A. Rudenko, L. Foucar, N. Kimmel, G. Weidenspointner, P. Holl, M. N. Liang, M. Barthelmess, C. Caleman, S. Boutet, M. J. Bogan, J. Krzywinski, C. Bostedt, S. Bajt, L. Gumprecht, B. Rudek, B. Erk, C. Schmidt, A. Homke, C. Reich, D. Pietschner, L. Struder, G. Hauser, H. Gorke, J. Ullrich, S. Herrmann, G. Schaller, F. Schopper, H. Soltau, K. U. Kuhnel, M. Messerschmidt, J. D. Bozek, S. P. Hau-Riege,

M. Frank, C. Y. Hampton, R. G. Sierra, D. Starodub, G. J. Williams, J. Hajdu, N. Timneanu, M. M. Seibert, J. Andreasson, A. Rocker, O. Jonsson, M. Svenda, S. Stern, K. Nass, R. Andritschke, C. D. Schroter, F. Krasniqi, M. Bott, K. E. Schmidt, X. Y. Wang, I. Grotjohann, J. M. Holton, T. R. M. Barends, R. Neutze, S. Marchesini, R. Fromme, S. Schorb, D. Rupp, M. Adolph, T. Gorkhover, I. Andersson, H. Hirsemann, G. Potdevin, H. Graafsma, B. Nilsson, and J. C. H. Spence, "Femtosecond X-ray protein nanocrystallography," Nature **470**, 73 (2011).

[2]R. Neutze, R. Wouts, D. van der Spoel, E. Weckert, and J. Hajdu, "Potential for biomolecular imaging with femtosecond X-ray pulses," Nature **406**, 752 (2000).

[3]A. Barty, C. Caleman, A. Aquila, N. Timneanu, L. Lomb, T. A. White, J. Andreasson, D. Arnlund, S. Bajt, T. R. M. Barends, M. Barthelmess, M. J. Bogan, C. Bostedt, J. D. Bozek, R. Coffee, N. Coppola, J. Davidsson, D. P. DePonte, R. B. Doak, T. Ekeberg, V. Elser, S. W. Epp, B. Erk, H. Fleckenstein, L. Foucar, P. Fromme, H. Graafsma, L. Gumprecht, J. Hajdu, C. Y. Hampton, R. Hartmann, A. Hartmann, G. Hauser, H. Hirsemann, P. Holl, M. S. Hunter, L. Johansson, S. Kassemeyer, N. Kimmel, R. A. Kirian, M. Liang, F. R. N. C. Maia, E. Malmerberg, S. Marchesini, A. V. Martin, K. Nass, R. Neutze, C. Reich, D. Rolles, B. Rudek, A. Rudenko, H. Scott, I. Schlichting, J. Schulz, M. M. Seibert, R. L. Shoeman, R. G. Sierra, H. Soltau, J. C. H. Spence, F. Stellato, S. Stern, L. Strueder, U. Weierstall, C. B. Wunderer, and H. N. Chapman, "Self-terminating diffraction gates femtosecond X-ray nanocrystallography measurements," Nat. Photonics **6**, 35 (2012).

[4]L. Lomb, T. R. M. Barends, S. Kassemeyer, A. Aquila, S. W. Epp, B. Erk, L. Foucar, R. Hartmann, B. Rudek, D. Rolles, A. Rudenko, R. L. Shoeman, J. Andreasson, S. Bajt, M. Barthelmess, A. Barty, M. J. Bogan, C. Bostedt, J. D. Bozek, C. Caleman, R. Coffee, N. Coppola, D. P. Deponte, R. B. Doak, T. Ekeberg, H. Fleckenstein, P. Fromme, M. Gebhardt, H. Graafsma, L. Gumprecht, C. Y. Hampton, A. Hartmann, G. Hauser, H. Hirsemann, P. Holl, J. M. Holton, M. S. Hunter, W. Kabsch, N. Kimmel, R. A. Kirian, M. Liang, F. R. N. C. Maia, A. Meinhart, S. Marchesini, A. V. Martin, K. Nass, C. Reich, J. Schulz, M. M. Seibert, R. Sierra, H. Soltau, J. C. H. Spence, J. Steinbrener, F. Stellato, S. Stern, N. Timneanu, X. Wang, G. Weidenspointner, U. Weierstall, T. A. White, C. Wunderer, H. N. Chapman, J. Ullrich, L. Strüder, and I. Schlichting, "Radiation damage in protein serial femtosecond crystallography using an X-ray free-electron laser," Phys. Rev. B **84**, 214111 (2011).

[5]W. Liu, D. Wacker, C. Gati, G. W. Han, D. James, D. Wang, G. Nelson, U. Weierstall, V. Katritch, A. Barty, N. A. Zatsepin, D. Li, M. Messerschmidt, S. Boutet, G. J. Williams, J. E. Koglin, M. M. Seibert, C. Wang, S. T. A. Shah, S. Basu, R. Fromme, C. Kupitz, K. N. Rendek, I. Grotjohann, P. Fromme, R. A. Kirian, K. R. Beyerlein, T. A. White, H. N. Chapman, M. Caffrey, J. C. H. Spence, R. C. Stevens, and V. Cherezov, "Serial femtosecond crystallography of G protein–coupled receptors," Science **342**, 1521 (2013).

[6]S. Boutet, L. Lomb, G. J. Williams, T. R. M. Barends, A. Aquila, R. B. Doak, U. Weierstall, D. P. DePonte, J. Steinbrener, R. L. Shoeman, M. Messerschmidt, A. Barty, T. A. White, S. Kassemeyer, R. A. Kirian, M. M. Seibert, P. A. Montanez, C. Kenney, R. Herbst, P. Hart, J. Pines, G. Haller, S. M. Gruner, H. T. Philipp, M. W. Tate, M. Hromalik, L. J. Koerner, N. van Bakel, J. Morse, W. Ghonsalves, D. Arnlund, M. J. Bogan, C. Caleman, R. Fromme, C. Y. Hampton, M. S. Hunter, L. C. Johansson, G. Katona, C. Kupitz, M. Liang, A. V. Martin, K. Nass, L. Redecke, F. Stellato, N. Timneanu, D. Wang, N. A. Zatsepin, D. Schafer, J. Defever, R. Neutze, P. Fromme, J. C. H. Spence, H. N. Chapman, and I. Schlichting, "High-resolution protein structure determination by serial femtosecond crystallography," Science **337**, 362 (2012).

[7]L. Redecke, K. Nass, D. P. DePonte, T. A. White, D. Rehders, A. Barty, F. Stellato, M. Liang, T. R. M. Barends, S. Boutet, G. J. Williams, M. Messerschmidt, M. M. Seibert, A. Aquila, D. Arnlund, S. Bajt, T. Barth, M. J. Bogan, C. Caleman, T.-C. Chao, R. B. Doak, H. Fleckenstein, M. Frank, R. Fromme, L. Galli, I. Grotjohann, M. S. Hunter, L. C. Johansson, S. Kassemeyer, G. Katona, R. A. Kirian, R. Koopmann, C. Kupitz, L. Lomb, A. V. Martin, S. Mogk, R. Neutze, R. L. Shoeman, J. Steinbrener, N. Timneanu, D. Wang, U. Weierstall, N. A. Zatsepin, J. C. H. Spence, P. Fromme, I. Schlichting, M. Duszenko, C. Betzel, and H. N. Chapman, "Natively inhibited trypanosoma brucei cathepsin B structure determined by using an X-ray laser," Science **339**, 227 (2013).

[8]M. Suga, F. Akita, K. Hirata, G. Ueno, H. Murakami, Y. Nakajima, T. Shimizu, K. Yamashita, M. Yamamoto, H. Ago, and J.-R. Shen, "Native structure of photosystem II at 1.95 Å resolution viewed by femtosecond X-ray pulses," Nature **517**, 99 (2014).

[9]T. R. M. Barends, L. Foucar, S. Botha, R. B. Doak, R. L. Shoeman, K. Nass, J. E. Koglin, G. J. Williams, S. Boutet, M. Messerschmidt, and I. Schlichting, "De novo protein crystal structure determination from X-ray free-electron laser data," Nature **505**, 244 (2014).

[10]L. C. Johansson, D. Arnlund, G. Katona, T. A. White, A. Barty, D. P. DePonte, R. L. Shoeman, C. Wickstrand, A. Sharma, G. J. Williams, A. Aquila, M. J. Bogan, C. Caleman, J. Davidsson, R. B. Doak, M. Frank, R. Fromme, L. Galli, I. Grotjohann, M. S. Hunter, S. Kassemeyer, R. A. Kirian, C. Kupitz, M. Liang, L. Lomb, E. Malmerberg, A. V. Martin, M. Messerschmidt, K. Nass, L. Redecke, M. M. Seibert, J. Sjöhamn, J. Steinbrener, F. Stellato, D. Wang, W. Y. Wahlgren, U. Weierstall, S. Westenhoff, N. A. Zatsepin, S. Boutet, J. C. H. Spence, I. Schlichting, H. N. Chapman, P. Fromme, and R. Neutze, "Structure of a photosynthetic reaction centre determined by serial femtosecond crystallography," Nat. Commun. **4**, 2911 (2013).

[11]A. Aquila, M. S. Hunter, R. B. Doak, R. A. Kirian, P. Fromme, T. A. White, J. Andreasson, D. Arnlund, S. Bajt, T. R. M. Barends, M. Barthelmess, M. J. Bogan, C. Bostedt, H. Bottin, J. D. Bozek, C. Caleman, N. Coppola, J. Davidsson, D. P. DePonte, V. Elser, S. W. Epp, B. Erk, H. Fleckenstein, L. Foucar, M. Frank, R. Fromme, H. Graafsma, I. Grotjohann, L. Gumprecht, J. Hajdu, C. Y. Hampton, A. Hartmann, R. Hartmann, S. Hau-Riege, G. Hauser, H. Hirsemann, P. Holl, J. M. Holton, A. H. Mke, L. Johansson, N. Kimmel, S. Kassemeyer, F. Krasniqi, K.-U. K. Hnel, M. Liang, L. Lomb, E. Malmberg, S. Marchesini, A. V. Martin, F. R. N. C. Maia, M. Messerschmidt, K. Nass, C. Reich, R. Neutze, D. Rolles, B. Rudek, A. Rudenko, I. Schlichting, C. Schmidt, K. E. Schmidt, J. Schulz, M. M. Seibert, R. L. Shoeman, R. Sierra, H. Soltau, D. Starodub, F. Stellato, S. Stern, L. Struder, N. Timneanu, J. Ullrich, X. Wang, G. J. Williams, G. Weidenspointner, U. Weierstall, C. Wunderer, A. Barty, J. C. H. Spence, and H. N. Chapman, "Time-resolved protein nanocrystallography using an X-ray free-electron laser," Opt. Express **20**, 2706 (2012).

[12]D. Arnlund, L. C. Johansson, C. Wickstrand, A. Barty, G. J. Williams, E. Malmerberg, J. Davidsson, D. Milathianaki, D. P. DePonte, R. L. Shoeman, D. Wang, D. James, G. Katona, S. Westenhoff, T. A. White, A. Aquila, S. Bari, P. Berntsen, M. Bogan, T. B. van driel, R. B. Doak, K. S. Kjær, M. Frank, R. Fromme, I. Grotjohann, R. Henning, M. S. Hunter, R. A. Kirian, I. Kosheleva, C. Kupitz, M. Liang, A. V. Martin, M. M. Nielsen, M. Messerschmidt, M. M. Seibert, J. Sjöhamn, F. Stellato, U. Weierstall, N. A. Zatsepin, J. C. H. Spence, P. Fromme, I. Schlichting, S. Boutet, G. Groenhof, H. N. Chapman, and R. Neutze, "Visualizing a protein quake with time-resolved X-ray scattering at a free-electron laser," Nat. Methods **11**, 923 (2014).

[13]C. Kupitz, S. Basu, I. Grotjohann, R. Fromme, N. A. Zatsepin, K. N. Rendek, M. S. Hunter, R. L. Shoeman, T. A. White, D. Wang, D. James, J.-H. Yang, D. E. Cobb, B. Reeder, R. G. Sierra, H. Liu, A. Barty, A. L. Aquila, D. Deponte, R. A. Kirian, S. Bari, J. J. Bergkamp, K. R. Beyerlein, M. J. Bogan, C. Caleman, T.-C. Chao, C. E. Conrad, K. M. Davis, H. Fleckenstein, L. Galli, S. P. Hau-Riege, S. Kassemeyer, H. Laksmono, M. Liang, L. Lomb, S. Marchesini, A. V. Martin, M. Messerschmidt, D. Milathianaki, K. Nass, A. Ros, S. Roy-Chowdhury, K. Schmidt, M. Seibert, J. Steinbrener, F. Stellato, L. Yan, C. Yoon, T. A. Moore, A. L. Moore, Y. Pushkar, G. J. Williams, S. Boutet, R. B. Doak, U. Weierstall, M. Frank, H. N. Chapman, J. C. H. Spence, and P. Fromme, "Serial time-resolved crystallography of photosystem II using a femtosecond X-ray laser," Nature **513**, 261 (2014).

[14]J. Kern, R. Alonso-Mori, R. Tran, J. Hattne, R. J. Gildea, N. Echols, C. Glöckner, J. Hellmich, H. Laksmono, R. G. Sierra, B. Lassalle-Kaiser, S. Koroidov, A. Lampe, G. Han, S. Gul, D. Difiore, D. Milathianaki, A. R. Fry, A. Miahnahri, D. W. Schafer, M. Messerschmidt, M. M. Seibert, J. E. Koglin, D. Sokaras, T.-C. Weng, J. Sellberg, M. J. Latimer, R. W. Grosse-Kunstleve, P. H. Zwart, W. E. White, P. Glatzel, P. D. Adams, M. J. Bogan, G. J. Williams, S. Boutet, J. Messinger, A. Zouni, N. K. Sauter, V. K. Yachandra, U. Bergmann, and J. Yano, "Simultaneous femtosecond X-ray spectroscopy and diffraction of photosystem II at room temperature," Science **340**, 491 (2013).

[15]J. Tenboer, S. Basu, N. Zatsepin, K. Pande, D. Milathianaki, M. Frank, M. Hunter, S. Boutet, G. J. Williams, J. E. Koglin, D. Oberthuer, M. Heymann, C. Kupitz, C. Conrad, J. Coe, S. Roy-Chowdhury, U. Weierstall, D. James, D. Wang, T. Grant, A. Barty, O. Yefanov, J. Scales, C. Gati, C. Seuring, V. Srajer, R. Henning, P. Schwander, R. Fromme, A. Ourmazd, K. Moffat, J. J. Van Thor, J. C. H. Spence, P. Fromme, H. N. Chapman, and M. Schmidt, "Time-resolved serial crystallography captures high-resolution intermediates of photoactive yellow protein," Science **346**, 1242 (2014).

[16]U. Weierstall, "Liquid sample delivery techniques for serial femtosecond crystallography," Philos. Trans. R. Soc., B **369**, 20130337 (2014).

[17]D. P. DePonte, U. Weierstall, K. Schmidt, J. Warner, D. Starodub, J. C. H. Spence, and R. B. Doak, "Gas dynamic virtual nozzle for generation of microscopic droplet streams," J. Phys. D **41**, 195505 (2008).

[18]U. Weierstall, J. C. H. Spence, and R. B. Doak, "Injector for scattering measurements on fully solvated biospecies," Rev. Sci. Instrum. **83**, 035108 (2012).

[19]A. J. Acero, C. Ferrera, J. M. Montanero, and A. M. Gañán-Calvo, "Focusing liquid microjets with nozzles," J. Micromech. Microeng. **22**, 065011 (2012).

[20]A. Gañán-Calvo and J. Montanero, "Revision of capillary cone-jet physics: Electrospray and flow focusing," Phys. Rev. E **79**, 066305 (2009).

[21]J. M. Montanero, A. M. Gañán-Calvo, A. J. Acero, and E. J. Vega, "Micrometer glass nozzles for flow focusing," J. Micromech. Microeng. **20**, 075035 (2010).

[22]J. M. Montanero, N. Rebollo-Muñoz, M. A. Herrada, and A. M. Gañán-Calvo, "Global stability of the focusing effect of fluid jet flows," Phys. Rev. E **83**, 036309 (2011).

[23]E. J. Vega, J. M. Montanero, M. A. Herrada, and A. M. Gañán-Calvo, "Global and local instability of flow focusing: The influence of the geometry," Phys. Fluids **22**, 064105 (2010).

[24]A. M. Gañán-Calvo, "Generation of steady liquid microthreads and micron-sized monodisperse sprays in gas streams," Phys. Rev. Lett. **80**, 285 (1998).

[25]M. Trebbin, K. Krüger, D. Deponte, S. V. Roth, H. N. Chapman, and S. Förster, "Microfluidic liquid jet system with compatibility for atmospheric and high-vacuum conditions," Lab Chip **14**, 1733 (2014).

[26]J. N. Tilton, in *Perry's Chemical Engineers' Handbook*, 7th ed., edited by D. W. Green and J. O. Maloney (McGraw-Hill, New York, 1999), pp. 6-21–6-23.

[27]Spacer design was inspired by pieces originally manufactured by A. Schleifer of Agilent Technologies, in Collaboration with B. Doak, U. Weierstall, and J. H. C. Spence of Arizona State University (2014).

[28]J. M. Montanero, M. A. Herrada, C. Ferrera, E. J. Vega, and A. M. Gañán-Calvo, "On the validity of a universal solution for viscous capillary jets," Phys. Fluids **23**, 122103 (2011).

[29]T. Si, F. Li, X.-Y. Yin, and X.-Z. Yin, "Modes in flow focusing and instability of coaxial liquid–gas jets," J. Fluid Mech. **629**, 1 (2009).

[30]S. Boutet and G. J. Williams, "The coherent X-ray imaging (CXI) instrument at the linac coherent light source (LCLS)," New J. Phys. **12**, 035024 (2010).

[31]F. Stellato, D. Oberthür, M. Liang, R. Bean, C. Gati, O. Yefanov, A. Barty, A. Burkhardt, P. Fischer, L. Galli, R. A. Kirian, J. Meyer, S. Panneerselvam, C. H. Yoon, F. Chervinskii, E. Speller, T. A. White, C. Betzel, A. Meents, and H. N. Chapman, "Room-temperature macromolecular serial crystallography using synchrotron radiation," IUCrJ **1**, 204 (2014).

[32]U. Weierstall, D. James, C. Wang, T. A. White, D. Wang, W. Liu, J. C. H. Spence, R. Bruce Doak, G. Nelson, P. Fromme, R. Fromme, I. Grotjohann, C. Kupitz, N. A. Zatsepin, H. Liu, S. Basu, D. Wacker, D. Won Han, V. Katritch, S. Boutet, M. Messerschmidt, G. J. Williams, J. E. Koglin, M. Marvin seibert, M. Klinker, C. Gati, R. L. Shoeman, A. Barty, H. N. Chapman, R. A. Kirian, K. R. Beyerlein, R. C. Stevens, D. Li, S. T. A. Shah, N. Howe, M. Caffrey, and V. Cherezov, "Lipidic cubic phase injector facilitates membrane protein serial femtosecond crystallography," Nat. Commun. **5**, 3309 (2014).